Materials Today Bio 20 (2023) 100670

Contents lists available at ScienceDirect

Materials Today Bio

journal homepage: www.journals.elsevier.com/materials-today-bio

Microfluidic synthesis of fibronectin-coated polydopamine nanocomplexes for self-supplementing tumor microenvironment regulation and MR imaging-guided chemo-chemodynamic-immune therapy

Rui Yang [a], Mengsi Zhan [a], Zhijun Ouyang [a], Honghua Guo [b], Jiao Qu [b], Jindong Xia [b], Mingwu Shen [a], Xiangyang Shi [a,*]

[a] State Key Laboratory for Modification of Chemical Fibers and Polymer Materials, Shanghai Engineering Research Center of Nano-Biomaterials and Regenerative Medicine, College of Biological Science and Medical Engineering, Donghua University, Shanghai, 201620, PR China
[b] Department of Radiology, Shanghai Songjiang District Central Hospital, Shanghai, 201600, PR China

ARTICLE INFO

Keywords:
Polydopamine iron nanocomplex
Microfluidic synthesis
Tumor microenvironment regulation
Enhanced chemodynamic therapy
Immune checkpoint blockade

ABSTRACT

Development of nanomedicines to overcome the hindrances of tumor microenvironment (TME) for tumor theranostics with alleviated side effects remains challenging. We report here a microfluidic synthesis of artesunate (ART)-loaded polydopamine (PDA)/iron (Fe) nanocomplexes (NCs) coated with fibronectin (FN). The created multifunctional Fe-PDA@ART/FN NCs (FDRF NCs) with a mean size of 161.0 nm exhibit desired colloidal stability, monodispersity, r_1 relaxivity (4.96 $mM^{-1}s^{-1}$), and biocompatibility. The co-delivery of the Fe^{2+} and ART enables enhanced chemodynamic therapy (CDT) through improved intracellular reactive oxygen species generation *via* a cycling reaction between Fe^{3+} and Fe^{2+} caused by the Fe^{3+}-mediated glutathione oxidation and Fe^{2+}-mediated ART reduction/Fenton reaction for self-supplementing TME regulation. Likewise, the combination of ART-mediated chemotherapy and the Fe^{2+}/ART-regulated enhanced CDT enables noticeable immunogenic cell death, which can be collaborated with antibody-mediated immune checkpoint blockade to exert immunotherapy having significant antitumor immunity. The combined therapy improves the efficacy of primary tumor therapy and tumor metastasis inhibition by virtue of FN-mediated specific targeting of FDRF NCs to tumors with highly expressed $\alpha_v\beta_3$ integrin and can be guided through the Fe(III)-rendered magnetic resonance (MR) imaging. The developed FDRF NCs may be regarded as an advanced nanomedicine formulation for chemo-chemodynamic-immune therapy of different tumor types under MR imaging guidance.

1. Introduction

Targeting and killing cancer cells while being blind to normal cells still faces great challenges in clinical practice [1,2]. In comparison with normal tissues, tumor microenvironment (TME) exhibits many distinctive characteristics including weakly acidic pH, hypoxia, high contents of reactive oxygen species (ROS) and glutathione (GSH), and immune imbalance, which are likely major factors of drug resistance and the main obstacles for current tumor treatments [3–6]. Nevertheless, in another perspective, the tumor-specific features in TME may turn to be a promising target for improved tumor theranostics [7,8]. Promisingly, chemodynamic therapy (CDT), a highly selective and endogenously activated treatment modality, has shown enormous potential in tumor-specific treatment with reduced systemic toxic side effects [9,10]. In particular, transition metal-based nanomaterials dissociate metal ions to initiate the Fenton or Fenton-like reaction with hydrogen peroxide (H_2O_2) to generate a large number of lethal hydroxyl radicals (·OH, a kind of ROS) under the hypoxic TME, triggering cell apoptosis and realizing CDT of cancer [11,12]. However, overexpressed GSH (2–10 mM) [13] and relatively low H_2O_2 content (~100 μM) [14,15] in TME severely constrain the efficacy of CDT *via* effectively consuming ROS and reducing ROS generation, respectively. Hence, it is vital to enhance CDT through controllable TME regulation or improved ROS generation, and CDT-based multimodal synergistic therapy has shown a great potential to improve cancer treatment efficacy [16–19].

Artesunate (ART), a derivative of traditional Chinese medicine artemisinin with endoperoxide bridge, has demonstrated anticancer activity and negligible toxic side effects [20]. Notably, the endoperoxide bridge

* Corresponding author.
E-mail address: xshi@dhu.edu.cn (X. Shi).

https://doi.org/10.1016/j.mtbio.2023.100670
Received 29 April 2023; Received in revised form 12 May 2023; Accepted 18 May 2023
Available online 18 May 2023

of ART can be reduced by Fe^{2+} to generate highly toxic superoxide radicals ($\cdot O_2^-$, a kind of ROS), inducing apoptosis of cancer cells *via* lipid peroxidation, and proteins and DNA damages [20,21]. Hence, ART has been applied to achieve highly efficient CDT by increasing intracellular ROS and avoiding the deficiency of H_2O_2 in TME. However, hydrophobic nature, instability, inferior pharmacokinetics, poor bioavailability and non-specificity limit the direct utilization of ART in tumor treatment [22–24]. Although various ART-based nanoplatforms have been developed for tumor treatment, the non-specificity, single modal treatment or endogenous Fe^{2+}-stimulated ROS generation alone significantly limits their therapeutic efficacy [25–27].

To improve the CDT efficiency, a co-delivery nanoplatform of dihydroartemisinin (a derivative of artemisinin) and transferrin (a Fe^{3+} carrier) has been developed to enhance the intracellular ROS generation [28]. Apparently, Fe^{2+} can interact with ART and H_2O_2 to produce ROS and Fe^{3+}, respectively. Owing to the overexpressed GSH in TME, the produced Fe^{3+} can be reduced to Fe^{2+}, further enhancing ROS generation by Fe^{2+}-mediated ART reduction and Fenton reaction [29]. Meanwhile, the Fe^{3+}-mediated GSH depletion can reduce the ROS loss to sensitize the therapeutic efficiency of cancer cells [30]. Interestingly, based on the Fe^{3+}-mediated GSH oxidation and Fe^{2+}-mediated ART reduction/Fenton reaction, a classic cycling reaction between Fe^{3+} and Fe^{2+} could be realized, resulting in self-supplementing and sustained ROS generation and GSH depletion to modulate TME for enhanced cancer treatment. Furthermore, due to the r_1 relaxivity of Fe^{3+}, the Fe^{2+}-mediated ART reduction/Fenton reaction also allows the generation of Fe^{3+} for T_1-weighted magnetic resonance (MR) imaging applications. In any case, according to our literature investigation, there is currently no co-delivery nanoplatforms developed for both ART and Fe^{2+}.

Single modal treatment is hardly enough to deal with the complexity, heterogeneity and resistance of tumors. Obviously, both CDT and chemotherapy have been proven to induce antitumor immune responses through triggering immunogenic cell death (ICD) of tumor cells [18,31]. Simultaneously, compared to CDT or chemotherapy alone, the enhanced CDT and CDT-based synergistic therapy can further profoundly amplify ICD, enhancing antitumor immune responses [32–34]. Undergoing ICD, the tumor cells generally generate damage-associated molecular patterns (DAMPs) characterized by calreticulin (CRT) exposure on the surface of dying cells, subsequent high mobility group box 1 (HMGB1) release from cell nuclei, and adenosine triphosphate (ATP) secretion [31,35]. Furthermore, the DAMPs have been evidenced to effectively trigger dendritic cells (DCs) maturation and cytotoxic T lymphocytes infiltration in tumor tissues [36]. However, the tumor cells are generally able to evade recognition of T cells, due to the expressed programmed death-ligand 1 (PD-L1) on their surface [37]. Promisingly, immune checkpoint blockade (ICB) therapy based on PD-L1 antibody (A-PD-L1) can recover the tumor cell killing ability of T cells and systemic antitumor immunity to reverse the immune suppression of TME [38]. Meanwhile, due to the amplified ICD by cooperative CDT/chemotherapy, multimodal therapy nanoplatforms have been employed to synergize with ICB therapy to further boost the antitumor immunity and enhance antitumor efficacy [34,35].

In addition, nanoplatforms with tumor-specific targeting ability can further promote antitumor effects by enhancing the accumulation of nanomedicines at tumor sites. Fibronectin (FN), a dimeric glycoprotein of extracellular matrix, has good biocompatibility and can be easily modified [39]. In particular, due to the Arg-Gly-Asp peptide sequence at its central cell-binding domain, FN-based nanoplatforms can specifically target $\alpha_v\beta_3$ integrin-overexpressing cells [40,41]. Moreover, our previous work has demonstrated the FN-mediated tumor targeting through development of an FN-coated Fe^{3+}-phenolic network for cooperative tumor chemotherapy and CDT [18].

Obviously, high-quality nanoplatforms with specific targeting property for efficient drug delivery play a vital role in tumor diagnosis and precision therapy [42]. Nevertheless, it still poses a huge challenge to simply fabricate "all-in-one" nanoplatforms with multiple compositions, homogeneity, and stability for tumor theranostics, thus retarding the clinical translation of nanomedicines [43]. For chemical synthesis of nanoplatforms, microfluidics has been evidenced to precisely control the multicomponent reactions, composition, shape, and size distribution of nanoplatforms through controlling the reaction kinetics, reaction fluids, fluids mixing, and temperature [44]. Thus, microfluidics has been applied to manufacture a variety of high-quality nanoplatforms based on porous silicon [45], ultrasmall superparamagnetic iron oxide [46], gold [47], and lipid for tumor theranostics [48]. Particularly, for the efficient manufacture of nanoplatforms, the microvortices caused by regulating the flow rate ratio (FRR) of side inlets to middle inlet enable the controlled and rapid mixing of input streams, resulting in effective encapsulation of all components and tuning to reach the optimal ratios [49]. For instance, a recent work by Liu and co-workers showed the fabrication of an exosome membrane-coated poly (lactic-*co*-glycolic acid) nanoplatform *via* a microvortices strategy for targeted imaging of tumors [50].

Herein, we propose to fabricate ART-loaded polydopamine (PDA)/iron (Fe) nanocomplexes (NCs) coated with FN through a microfluidic synthesis method for targeted MR imaging-guided combination chemo/chemodynamic/immune therapy of tumors (Scheme 1). The Fe-PDA@ART/FN (FDRF) NCs were manufactured by rapid interfacial precipitation, diffusion and convective mixing based on a three stage-microfluidic chip. The developed FDRF NCs were systematically characterized and tested for theranostics of a xenografted 4T1 tumor mouse model through self-supplementing and sustained regulation of TME. The major innovation of the created FDRF NCs lies in the following aspects: (1) the FN-mediated targeting co-delivery of ART and Fe^{2+} can be achieved to enhance CDT by the high-quality FDRF NCs manufactured *via* a microfluidic synthesis method; (2) the amplified ICD-mediated immune cell activation can be realized by the combination of ART-mediated chemotherapy and the enhanced CDT through the cycling reaction of Fe^{2+}-mediated ART reduction/Fenton reaction and the Fe^{3+}-mediated GSH oxidation for self-supplementing and sustained TME regulation; and (3) the FDRF NCs can achieve efficient T_1 MR imaging-guided cancer therapy by combination of A-PD-L1-mediated ICB and enhanced ICD-activated immune stimulation.

2. Experimental section

2.1. Microfluidic synthesis of FD NCs

To prepare FD NCs, at the first stage, a Tris buffer solution (124 mM, 4 mL·h^{-1}) and a mixture solution of $FeCl_2{\cdot}4H_2O$ (2.54 mg·mL^{-1}) and DA (24.28 mg·mL^{-1}) in water (0.2 mL·h^{-1}) sonicated for 5 min were respectively injected into the microfluidic chip through two middle inlets (1 and 2). Two Tris buffer solutions (124 mM, 21 mL·h^{-1}) and a Tris buffer solution (124 mM, 4 mL·h^{-1}) were injected into the microfluidic chip through two side inlets (3)*2 at the second stage and the middle inlet (4) at the third stage, respectively. The flow rates of all inlets were precisely adjusted by syringe pumps. The obtained FD dispersion was collected *via* the outlet, purified (centrifugation at 8000 rpm, 10 min), washed, redispersed in water, and stored at 4 °C for later use. A fraction of the FD NCs was lyophilized for characterizations.

2.2. Microfluidic synthesis of FDR NCs

To prepare FDR NCs, a Tris buffer solution (124 mM, 4 mL·h^{-1}) and a mixture solution of $FeCl_2{\cdot}4H_2O$ (2.54 mg·mL^{-1}) and DA (24.28 mg·mL^{-1}) in water (0.2 mL·h^{-1}) sonicated for 5 min were respectively injected into the microfluidic chip through two middle inlets at the first stage (1 and 2). Two mixtures of ethanol and Tris buffer solution (v/v = 1: 20) containing ART (0.19 mg·mL^{-1}, 21 mL·h^{-1}) were injected into the microfluidic chip through two side inlets (3)*2 at the second stage, respectively. A Tris buffer solution (124 mM, 4 mL·h^{-1}) was injected into the microfluidic chip through the middle inlet (4) at the third stage. The

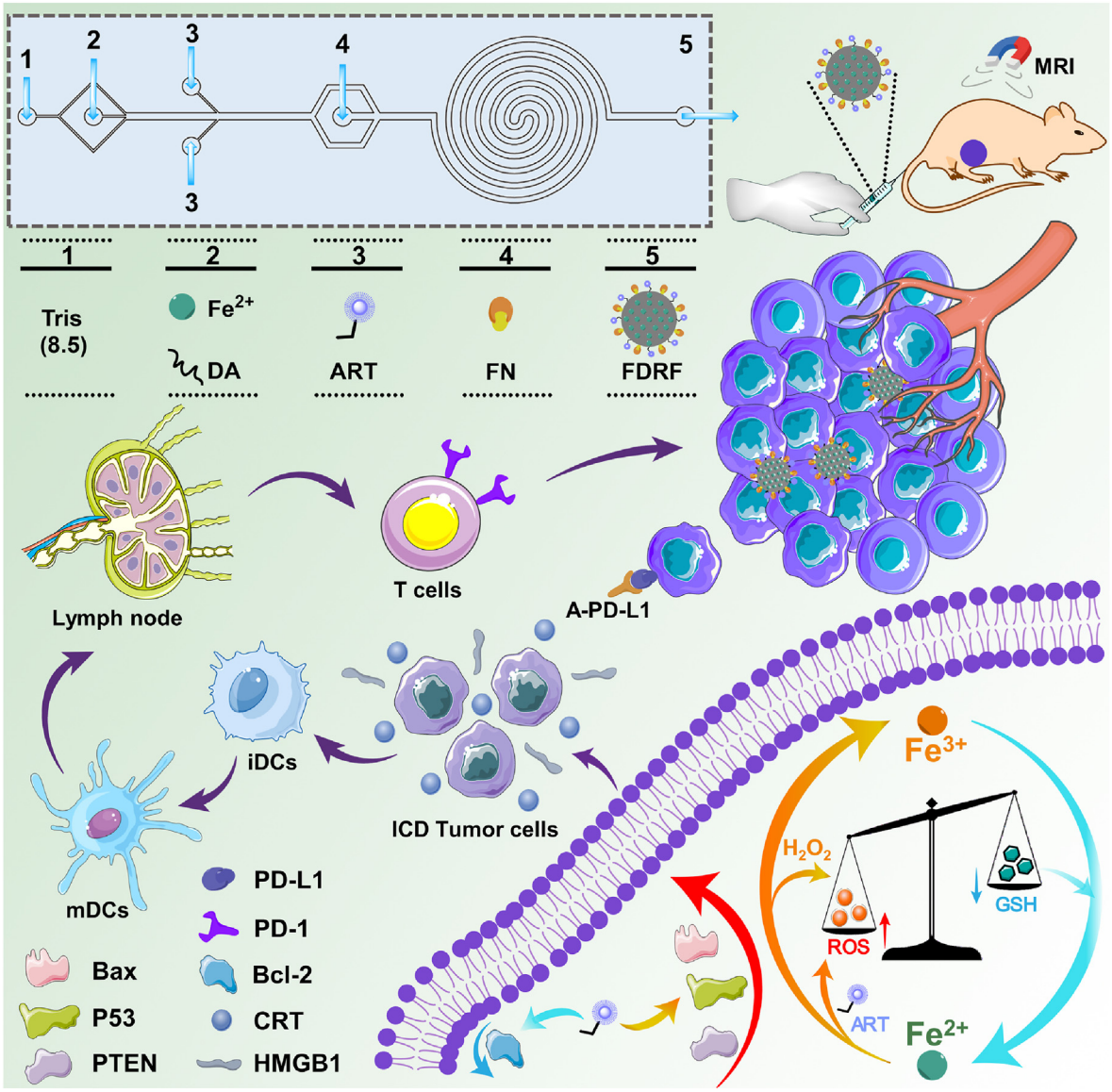

Scheme 1. Microfluidic synthesis of FDRF NCs for T_1 MR imaging and chemo-chemodynamic-immune therapy of tumors.

obtained FDR dispersion was collected *via* the outlet, purified (ultrafiltration centrifugation at 4500 rpm, 5 min), washed, redispersed in water, and stored at 4 °C for later use. A fraction of the FDR NCs was lyophilized for characterizations.

2.3. Microfluidic synthesis of FDRF NCs

To prepare FDRF NCs, at the first stage, a Tris buffer solution (124 mM, 4 $mL{\cdot}h^{-1}$) and a mixture solution of $FeCl_2{\cdot}4H_2O$ (2.54 $mg{\cdot}mL^{-1}$) and DA (24.28 $mg{\cdot}mL^{-1}$) in water (0.2 $mL{\cdot}h^{-1}$) sonicated for 5 min were respectively injected into the microfluidic chip through two middle inlets (1 and 2). Two mixtures of ethanol and Tris buffer solution (v/v = 1: 20) containing ART (0.19 $mg{\cdot}mL^{-1}$, 21 $mL{\cdot}h^{-1}$) were respectively injected into the microfluidic chip through two side inlets (3)*2 at the second stage. A 0.8 $mg{\cdot}mL^{-1}$ solution of FN in water (4 $mL{\cdot}h^{-1}$) was injected into the microfluidic chip through the middle inlet (4) at the third stage. The obtained FDRF dispersion was collected *via* the outlet, purified (centrifugation at 8000 rpm, 10 min), washed, redispersed in water, and stored at 4 °C for later use. A fraction of the FDRF NCs was lyophilized for characterizations.

2.4. Cell culture and in vitro assays

4T1 and L929 cells were regularly cultured, passaged and adopted for *in vitro* assays including CCK-8 cytotoxicity, cellular uptake, standard kit, flow cytometry, confocal microscopic observation of the intracellular ROS generation, GSH depletion and LPO accumulation, cell apoptosis, Western blotting, ICD, and DCs maturation.

2.5. Animal experiments

All animal experiments were performed after approval by the Ethical Committee for Experimental Animal Care and Use of Donghua University and also according to the guidelines and regulations of National Ministry of Health (China). Mouse blood was collected for hemolysis assay to evaluate the hemocompatibility of FDRF. Mouse 4T1 tumor model was established for MR imaging, biodistribution, and *in vivo* chemotherapy, enhanced CDT and immunotherapy evaluations. Histological examinations of major organs, blood routines and serum biochemistry tests were conducted to evaluate the biosafety of FDRF.

2.6. Statistical analysis

Experimental data are displayed as the mean ± standard deviation ($n \geq 3$). One-way analysis of variance statistical analysis was performed using GraphPad Prism 8.0.2 software (San Diego, CA) to evaluate the significance of the experimental data. In all cases, a p value of 0.05 was chosen as the significance level, and the data were marked with (*) for $p < 0.05$, (**) for $p < 0.01$, and (***) for $p < 0.001$, respectively. For full experimental details, see the Supporting Information.

3. Results and discussion

3.1. Synthesis and characterization of FDRF NCs

To manufacture the FDRF NCs, a microfluidic chip was designed [50–52] to contain three stages: a) the first stage consists of two inlets and a straight channel (the first inlet for introducing the Tris buffer solution, and the second inlet for the mixed aqueous solution of Fe^{2+} and dopamine (DA)); b) the second stage owns two side inlets for the mixture of ethanol and Tris buffer solution sheaths containing ART and one straight channel; and c) the third stage possess one center inlet for FN in water, and one double spiral mixing microfluidic channel (Figs. S1A–B and Scheme 1). In the present work, the Fe-PDA (FD) was firstly synthesized through an efficient and rapid interfacial precipitation method based on the microvortices generated by regulating the FRR (FRR = 20) at the first stage of the multi-stage microfluidic device. Furthermore, ART or ART/FN were assembled onto the outer surface of FD for the synthesis of Fe-PDA@ART (FDR) or FDRF through primary rapid interface diffusion and secondary convective mixing induced by regulating the FRR (second: FRR = 10, third: FRR = 11.5) at the second and third stage of microfluidic device, respectively. Meanwhile, the assembly was also assisted with the double spiral structure at the third stage of microfluidic channel [53,54]. For comparison, bovine serum albumin (BSA) without targeting ability was used as an alternative to FN and the Fe-PDA@ART/BSA (FDRB) NCs were prepared under the same conditions as FDRF NCs. In order to optimize the fabrication of FDRF, under varying DA/ART molar ratios, the loading capacity (LC) and encapsulation efficiency (EE) of ART in FDRF were calculated (Table S1). At the DA/ART molar ratio of 1.2: 1.0, the LC and EE of ART in the FDRF reach the optimal values of 38.1% and 55.0%, respectively. The synthesized NCs exhibit a spherical morphology and good monodispersity, which can be proven by transmission electron microscopy (TEM) imaging (Fig. S2 and Fig. 1A–C). Compared with FD with a mean diameter of 201.8 ± 9.4 nm (Fig. S2A), the loading of ART leads to a smaller size of the FDR NCs with a mean dimeter of 70.9 ± 11.9 nm (Fig. S2B), which may be due to the reaction of a portion of ART with Fe^{2+} on the surface of FD to shrink the particle volume. Further coating of BSA and FN brings the formation of mesoporous particles of FDRB with an average size of 121.3 ± 12.5 nm (Fig. S2C) and FDRF with a mean diameter of 161.0 ± 7.6 nm (Fig. 1C), respectively, which are both larger than that of FDR, implying the success of BSA or FN coating, which could be helpful to effectively protect ART from decomposition. Interestingly, compared to the FDRB NCs, the FDRF NCs display a more roundish and neat morphology, which might be due to the differences in the molecular weight and the number of amino or carboxyl groups between BSA and FN. It seems that FN with a larger molecular weight and number of amino or carboxyl groups has a better coating than BSA.

Subsequently, the FDRF NCs were characterized by various techniques. As displayed in Table S2, the FD, FDR, FDRB, and FDRF have hydrodynamic diameters of 219.1 ± 3.6, 113.1 ± 18.7, 140.9 ± 8.9, and 207.7 ± 4.7 nm, respectively, displaying similar changing tendency to that measured by TEM. After ART loading, the zeta potential of FD (−9.7 ± 0.5 mV) decreases to −12.6 ± 0.7 mV owing to the physical interaction with negatively charged ART with FD [20,29,55], and further decreases to −21.7 ± 1.7 mV or −23.7 ± 0.1 mV after being lastly coated with negatively charged BSA or FN *via* the Michael addition or Schiff base reaction between the abundant catechol groups on FD surface and amines and thiols of BSA or FN, respectively (Table S2 and Fig. 1D) [56].

UV–vis absorption spectra reveal the near infrared absorption band of FD at 600–800 nm and the typical protein absorption band at 280 nm associated with the coated BSA or FN, implicating the successful synthesis of FD and coating of BSA or FN, respectively (Fig. 1E and Fig. S3A). In order to reveal the structure of the FD, FDR, FDRB, and FDRF, Fourier transform infrared (FTIR) spectroscopy was performed (Fig. 1F and Fig. S3B). Apparently, the peak at 596 cm^{-1} is assigned to Fe–O bond of FD, and the band at 1504 cm^{-1} is attributed to the stretching vibration of indole structure of PDA, indicating the successful generation of FD. In addition, the peak at 1756 cm^{-1} can be attributed to the characteristic endoperoxide bridge (-C-O-O-C-) of ART [23], suggesting the successful loading of ART.

X-ray photoelectron spectroscopy (XPS) was carried out to further verify the synthesis of FDRF (Fig. 1G). For FD and FDR, four elements including Fe, O, C, and N appear in the XPS spectra. In the XPS spectra of FDRB and FDRF, the emerging S peaks indicate that BSA and FN have been successfully loaded (Fig. 1G and Fig. S4). The high-resolution XPS spectrum of Fe 2p for the FDRF NCs can be fitted to have six peaks at 711.2, 714.8, 720.0, 725.5, 728.8, and 733.4 eV that can be ascribed to Fe^{2+} $2p_{3/2}$, Fe^{3+} $2p_{3/2}$, Fe $2p_{3/2}$ satellite, Fe^{2+} $2p_{1/2}$, Fe^{3+} $2p_{1/2}$, and Fe $2p_{1/2}$ satellite, respectively, demonstrating the existence of Fe^{2+} in the FDRF (Fig. 1H). The existence of Fe^{3+} could be associated to the oxidation of a portion of Fe^{2+} on the surface of FDRF NCs. Furthermore, sodium dodecyl sulfate-polyacrylamide gel electrophoresis (SDS-PAGE) was utilized to prove the loading of BSA or FN in the FDRB or FDRF NCs (Fig. 1I). The FDR NCs do not show any protein bands, while both FDRB and FDRF exhibit protein bands belonging to BSA and FN, respectively, proving the successful formation of FDRB and FDRF NCs. To further confirm the feasibility of FDRF for biomedical applications, the colloidal stability of the FDRF NCs dispersed in phosphate buffered saline (PBS) was then examined by dynamic light scattering (Fig. S5). The hydrodynamic size of the NCs shows no significant changes during the monitoring period of one week, validating their excellent colloidal stability.

3.2. Drug release kinetics

Subsequently, the hydrodynamic sizes of FDRF NCs under different pHs (6.5 and 7.4) were detected to investigate their pH-mediated degradation property. As shown in Fig. 2A, under pH 6.5, the FDRF NCs display an apparent size distribution variation with the appearance of multiple peaks. Furthermore, the characteristic absorption of -C-O-O-C- for ART disappears in the FTIR spectrum of FDRF under pH = 6.5, presumably due to the Fe^{2+}-mediated reduction of ART (Fig. S6), confirming the pH-responsive dissociation of FDRF NCs.

The pH-sensitive release of Fe and ART from the FDRF NCs was examined under different pHs (Fig. 2B–C). Obviously, about 19.0% of Fe and 38.4% of ART are released from the FDRF NCs at 96 h under a slightly acidic condition (pH 6.5), which is around 2.0 and 1.5 times higher than the release of Fe (9.7%) and ART (24.9%) under a physiological environment (pH 7.4), respectively. This demonstrates that the FDRF NCs can be responsively dissociated to release both Fe^{2+} and ART for efficient tumor theranostics under the acidic TME, while exhibit a lower drug release rate under physiological conditions to achieve reduced toxic side effects.

3.3. T_1 MR relaxometry

The T_1 MR relaxometry of FD, FDR, and FDRF was tested under pH = 7.4. As can be seen in Fig. 2D, FDRF NCs possess a high r_1 of 4.96 $mM^{-1}s^{-1}$ with an excellent T_1 MR effect, which is similar to those of FD (Fig. S7A, 4.57 $mM^{-1}s^{-1}$) and FDR (Fig. S7B, 4.69 $mM^{-1}s^{-1}$), indicating that the loading of ART and FN has no appreciable effect on the relaxation rate of the NCs. Due to the pH-responsiveness of FDRF, under a weakly acidic conditions (pH 6.5), the T_1 MR relaxometry of FDRF was

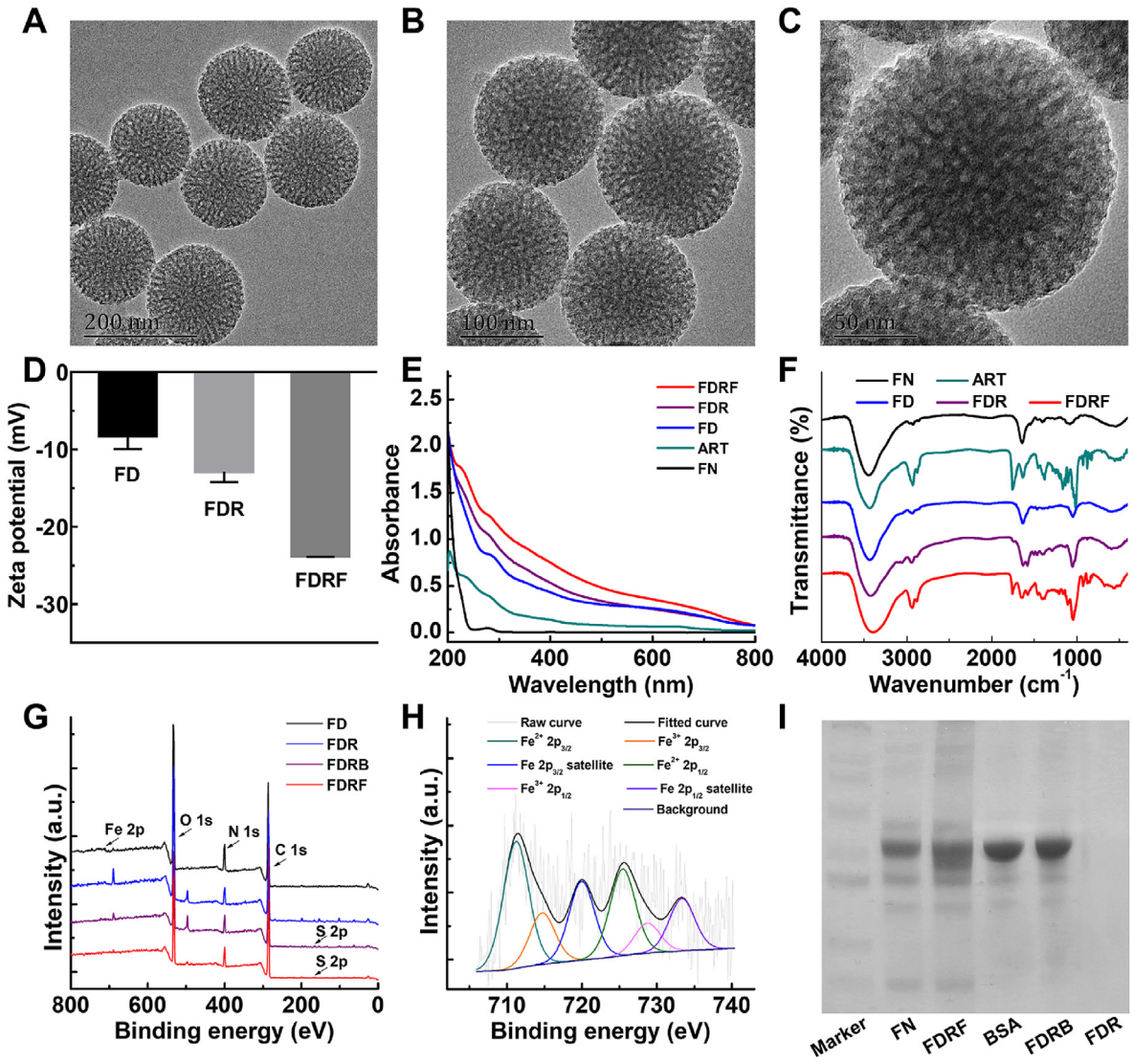

Fig. 1. Characterization of FDRF NCs. (A, B, and C) TEM images of FDRF NCs. (D) Zeta potentials of FD, FDR and FDRF NCs (n = 3). (E) UV–vis and (F) FTIR spectra of FN, ART, FD, FDR and FDRF. (G) XPS spectra of FD, FDR, FDRB and FDRF. (H) High-resolution XPS spectra of Fe 2p for FDRF. (I) SDS-PAGE analysis of FN, FDRF, BSA, FDRB and FDR.

further tested to explore the acid-enhanced T_1 MR effect (Fig. 2D). Notably, the r_1 of FDRF under pH 6.5 is 5.93 $mM^{-1}s^{-1}$, which is higher than that under pH 7.4 (4.96 $mM^{-1}s^{-1}$), showing that the developed FDRF NCs are endowed with enhanced T_1 MR imaging potential in the acidic TME, due to the increased release of Fe^{3+} caused by the dissociation of the NCs.

3.4. Detection of ROS generation

On one hand, Fe^{2+} can react with H_2O_2 *via* a Fenton reaction to produce ·OH [7], and on the other hand the endoperoxide bridges of ART can be reduced by Fe^{2+} to generate $\cdot O_2^-$ [21]. Then, an methylene blue (MB) degradation experiment was performed to explore the capacity of FDRF NCs to produce ROS under different conditions. As shown in Fig. S8 and Fig. 2E-F, the MB degradation occurs within 90 min under different conditions. In the absence of FDRF, MB is hardly degraded under physiological conditions (pH = 7.4) with or without H_2O_2. Nevertheless, the degradation of MB is improved to 16.9% and 26.3% in the presence of FDRF under pH 7.4 and pH 6.5, respectively, due to the Fe^{2+}-mediated reduction of the endoperoxide bridges of ART. Meanwhile, the higher degradation rate of MB under a slightly acidic condition than under pH 7.4 should be attributed to the pH-responsive of release of Fe^{2+} from the FDRF NCs. Lastly, under slightly acidic condition containing H_2O_2, the performance to amplify ROS generation of FDRF *via* dual pathways of Fenton reaction and ART reduction was confirmed. In such a case, the rate of MB degradation reaches 39.1%. Collectively, the developed FDRF NCs show an excellent CDT property based on the enhanced ROS generation *via* the dual-pathway strategy.

3.5. Cytotoxicity and cellular uptake assays in vitro

The cytotoxicity of FD, FDR, FDRB, FDRF and free ART was assayed with 4T1 cells to validate the anticancer activity of the FDRF NCs. We calculated the half maximal inhibitory concentrations (IC_{50}s) of FD, FDR, FDRB, FDRF and free ART to be 44.2, 8.2, 8.0, 5.2 and 34.3 μg·mL^{-1}, respectively (Fig. 2G and Fig. S9A). Apparently, the combined chemotherapy/enhanced CDT by the co-introduction of ART and Fe^{2+} (FDR, FDRB, and FDRF) exhibits much higher cytotoxicity than CDT alone (FD) or the combined chemotherapy/endogenous Fe^{2+}-activated CDT (ART). Cells treated with FD, FDR, FDRB, or FDRF at various Fe concentrations (1.25, 2.5, 5, 10, or 20 μg·mL^{-1}) display an Fe-dependent decrease of cell viability, and the FDRF NCs show the most remarkable anticancer effect

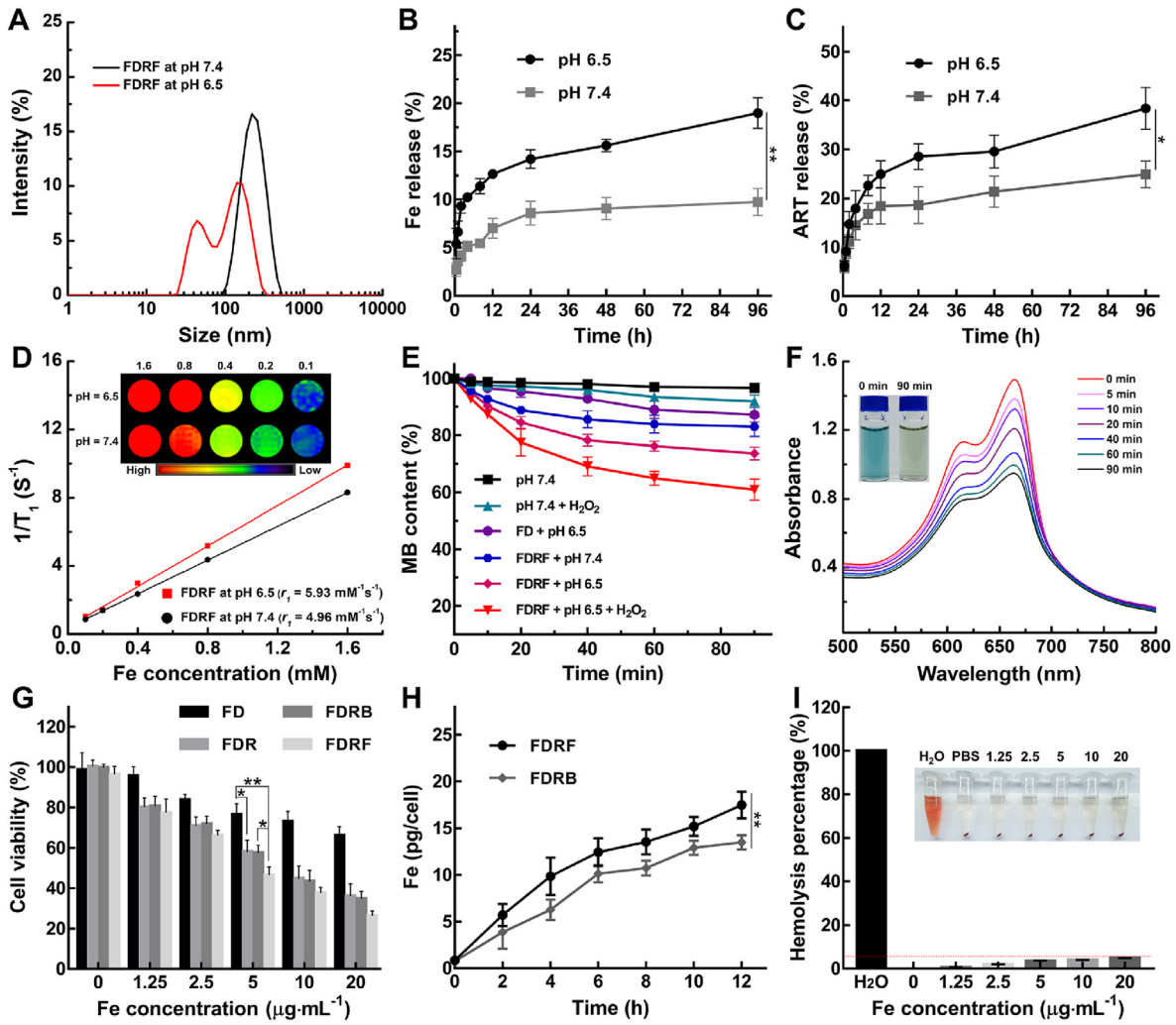

Fig. 2. The pH-responsiveness, ·OH generation, and cytotoxicity of FDRF NCs. (A) The hydrodynamic size of FDRF in phosphate buffer (pH = 6.5 or 7.4). Cumulative release of Fe (B) and ART (C) from FDRF NCs in phosphate buffer (pH = 6.5 or 7.4, n = 3). (D) T_1-weighted MR images and the corresponding plots of $1/T_1$ of FDRF versus Fe concentration ([Fe] = 0.1, 0.2, 0.4, 0.8 and 1.6 mM) under different pHs. (E) MB degradation ascribing to the ROS generation under different conditions with or without H_2O_2 (10 mM, n = 3). (F) Degradation process of MB at different time points after treated with FDRF (phosphate buffer (pH = 6.5), [H_2O_2] = 10 mM). (G) Viability of 4T1 cells treated with FD, FDR, FDRB or FDRF at different Fe concentrations for 24 h (n = 5). (H) Fe uptake in 4T1 cells treated with FDRB or FDRF ([Fe] = 10 μg·mL^{-1}) under different incubation time periods (n = 3). (I) Hemolysis percentage of MRBCs exposed to H_2O, PBS, and PBS containing FDRF at different Fe concentrations for 2 h (the red dotted line is the 5% reference safe line, n = 3). Inset shows a digital photograph of suspensions of MRBCs after different treatments, followed by centrifugation. In part B, C, G and H, * is for $p < 0.05$, and ** is for $p < 0.01$, respectively.

owing to the combined chemotherapy/enhanced CDT, and the enhanced cellular uptake (Fig. 2H) *via* the FN-mediated targeting. The FDR NCs ([Fe] = 5 μg·mL^{-1}) show a much stronger cytotoxicity than FD ($p < 0.05$), illustrating the superior anticancer activity of the combined chemotherapy/enhanced CDT based on the dual-pathway ROS generation. Similarly, the FDRF NCs display a higher cytotoxicity than the FDRB NCs at an Fe concentration of 5 μg·mL^{-1}, owing to the FN-mediated specific targeting to cancer cells having $\alpha_v\beta_3$ integrin overexpression ($p < 0.05$) [40].

To prove the FN-mediated enhanced cellular uptake of FDRF, the Fe contents of FDRF or FDRB taken up by 4T1 cells with $\alpha_v\beta_3$ integrin-expression were quantitatively tested through inductively coupled plasma-optical emission spectroscopy (ICP-OES). At the same Fe concentration (10 μg·mL^{-1}), cells incubated with FDRF or FDRB all show time-dependent uptake of Fe (Fig. 2H). Notably, compared to the non-targeted FDRB NCs, the FDRF NCs show much higher Fe uptake at the same time points, presumably owing to the FN-mediated targeting of FDRF toward $\alpha_v\beta_3$ integrin-expressing cancer cells.

To verify the biomedical applicability of FDRF NCs, we further examined their cytocompatibility and hemocompatibility using normal cells (L929 cells) and mouse red blood cells (MRBCs), respectively. As can be seen in Fig. S9B, L929 cells treated with FDRF or ART for 24 h show non-compromised cell viability in an ART concentration range of 0–49.6 μg·mL^{-1}, possibly owing to the less release of Fe and ART under the normal cellular microenvironment. Meanwhile, after treated with FDRF or ART, the viability of cells remains 86.9% or 85.4% at an ART concentration of 99.2 μg·mL^{-1}, further proving the cytocompatibility of FDRF.

Furthermore, hemolysis assay of MRBCs treated with the developed FDRF NCs was performed (Fig. 2I). In contrast to the positive control of H_2O having a 100% hemolysis rate, the MRBCs show a hemolysis rate below the threshold value of 5% after treated with FDRF at various Fe concentrations, approaching to the negative PBS control. Overall, the good cytocompatibility and hemocompatibility of the developed FDRF NCs were well proved.

3.6. ROS- and GSH-modulation in vitro

Then, the ROS- and GSH-modulation by FD, FDR, FDRB, FDRF and free ART were examined *in vitro*, respectively. Firstly, the ROS generation capacity of FD, FDR, FDRB, and FDRF at the same Fe concentration (20 $\mu g \cdot mL^{-1}$) and the ART concentration corresponding to the Fe-incorporated groups (99.2 $\mu g \cdot mL^{-1}$) was assessed in 4T1 cells by 2, 7-dichlorofluorescin diacetate (DCFH-DA) through flow cytometry (Fig. 3A and Fig. S10). It is clear that the FDRF NCs exhibit the strongest ROS generation capacity (132.1%) among all groups, suggesting their powerful TME regulation ability. Compared to the PBS control, improved ROS levels in cells treated with FD and ART can be achieved, presumably owing to the ·OH production *via* FD-promoted Fenton reaction in 4T1 cells containing excessive H_2O_2 and $\cdot O_2^-$ generation through endogenous Fe^{2+}-mediated reduction of ART, respectively. Interestingly, the ROS level of FDR group is higher than those of FD ($p < 0.001$) and ART ($p < 0.01$) groups, likely attributed to the dual-pathway amplified ROS generation through the exogenous/endogenous Fe^{2+}-induced Fenton reaction and reductive decomposition of ART. Compared to the FDRB group, the FDRF group shows a stronger ROS generation ($p < 0.01$), possibly due to the effect of FN-mediated targeting.

GSH, a ROS scavenger, can be directly oxidized by ROS and Fe^{3+} in

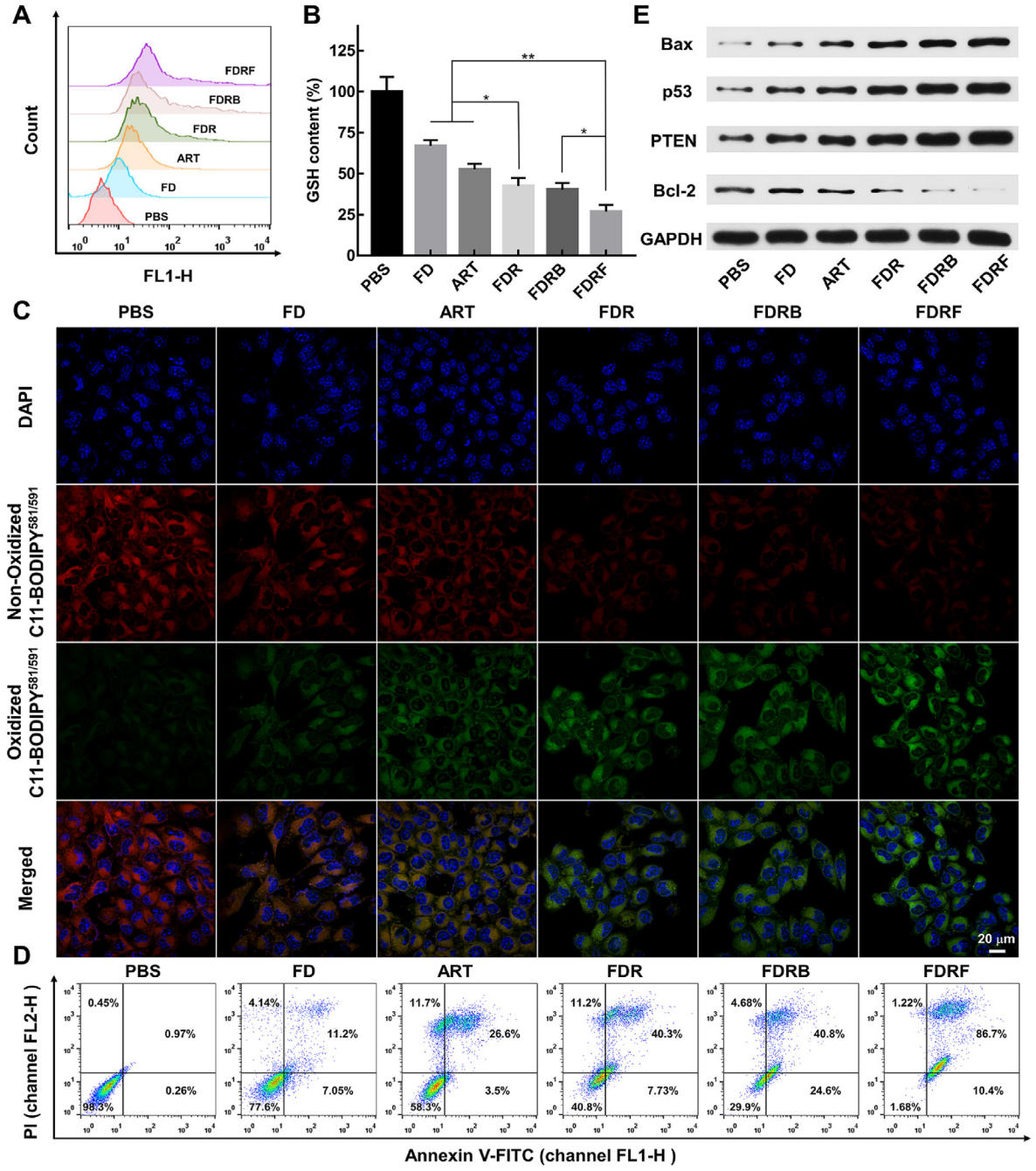

Fig. 3. Intracellular enhanced ROS generation of FDRF NCs. (A) Flow cytometry analysis of ROS generation in 4T1 cells treated by PBS, FD, ART, FDR, FDRB or FDRF for 6 h. (B) GSH content in 4T1 cells after different treatments for 6 h (n = 3). (C) CLSM images of lipid peroxide (LPO) in 4T1 cells after different treatments for 6 h (scale bar = 20 μm). Nuclei: blue. (D) Flow cytometry assay of 4T1 cell apoptosis after different treatments followed by staining with Annexin-FITC and PI. (E) Western blot analysis of the expression levels of Bax, p53, PTEN, and Bcl-2 after different treatments for 24 h. GAPDH was used as a reference. In part B, * is for $p < 0.05$, and ** is for $p < 0.01$, respectively.

TME [29]. The depletion of intracellular GSH can make tumor cells more susceptible to oxidative stress, chemotherapeutic drugs and ROS through weakening their antioxidative capacity [57], thus improving the anticancer effect [58]. Next, the GSH depletion ability of FD, FDR, FDRB, FDRF, and free ART at the same Fe concentration (20 μg·mL^{-1}) and the ART concentration corresponding to the Fe-incorporated groups (99.2 μg·mL^{-1}) was evaluated using 4T1 cells. Compared to the PBS group, all other groups show apparent depletion of GSH due to the mentioned ROS generation ability (Fig. 3B). Obviously, the FDR NCs exhibit a higher GSH consumption ability than FD and ART due to the dual-pathway improved ROS generation ($p < 0.05$) on one hand, and Fe^{3+} produced by both the Fe^{2+}-mediated Fenton reaction and reductive decomposition of ART on the other hand. Meanwhile, along with the consumption of GSH, Fe^{3+} can also be reduced to Fe^{2+}, indicating a probable cycling reaction between Fe^{3+} and Fe^{2+} resulting from GSH oxidation and both ART reduction and Fenton reaction (Scheme 1). Furthermore, the FDRF NCs exhibit the strongest ability to regulate TME with the highest GSH depletion (26.6%) by virtue of the FN-rendered specific targeting.

3.7. Intracellular LPO accumulation and cell apoptosis assays

Encouraged by the excellent capacity of FDRF to modulate TME for ROS generation and GSH depletion, we next explored the intracellular LPO accumulation and cancer cell apoptosis after cells were treated with the FDRF NCs. In comparison with the PBS control, other groups exhibit strengthened green fluorescence signals (oxidized C11-BODIPY$^{581/591}$) and corresponding attenuated red fluorescence signals (non-oxidized C11-BODIPY$^{581/591}$) in Fig. 3C, proving the NCs- and ART-induced LPO accumulation within the cancer cells. Compared to the FD and ART groups, much weaker red fluorescence signals and stronger green fluorescence signals of cells can be seen in the FDR-associated groups owing to the dual-pathway amplified ROS generation. Furthermore, cells treated with the FDRF NCs have the most effective LPO accumulation, owing to the FN-mediated specific targeting.

Subsequently, the FDRF-induced cell apoptosis effect was examined through flow cytometry. As shown in Fig. 3D, the sum of necrotic and apoptotic percentages of 4T1 cells treated with FDR (59.23%) is higher than that treated with the FD (22.39%) and ART (41.8%), suggesting the enhanced anticancer activity of FDR. Compared to the FDRB group (70.08%), the sum of necrotic and apoptotic percentages of 4T1 cells in the FDRF group (98.32%) increases dramatically, which should be owing to the improved endocytosis of the NCs *via* FN-mediated targeting. This further suggests that the FDRF NCs possess the highest anticancer efficacy among all groups, attributed to the combination of chemotherapy and enhanced CDT, and the specific targeting.

Furthermore, to elucidate the mechanism of the FDRF NC-caused cell apoptosis, proteins (Bax, p53, PTEN, and Bcl-2) associated to cell apoptosis were measured *via* Western blotting (Fig. 3E). The significant downregulation of antiapoptotic protein Bcl-2 and upregulation of both tumor suppressor p53/PTEN and proapoptotic protein Bax can be found after various treatments for 24 h, explaining the apoptosis pathway activation. Noticeably, the FDRF group displays the largest Bax/Bcl-2 ratio among all groups ($p < 0.001$), proving the tremendous potential of FDRF in the combination chemotherapy and enhanced CDT to treat cancer cells (Fig. S11).

3.8. ICD effect of FDRF NCs in vitro

As is known, ICD induced by chemotherapy and CDT has been reported to trigger dying cancer cells to generate DAMPs [33,59]. Encouraged by the excellent chemotherapy and enhanced CDT effect of the developed FDRF NCs, we next verified the *in vitro* ICD efficacy to confirm their immunity activation function. The characteristic ICD biomarkers in 4T1 cells after various treatments were detected, including ATP, HMGB1, and CRT. As shown in Fig. 4A–B, the released ATP and HMGB1 levels in the FDR group are remarkably higher than those in the FD ($p < 0.01$) and ART ($p < 0.01$) groups, indicating the improved ICD effect of FDR through the combination of chemotherapy and the enhanced CDT. Likewise, compared to the FD ($p < 0.05$) and ART ($p < 0.05$) groups, the FDR group shows significantly increased cell-surface CRT exposure (Fig. 4C). Meanwhile, as shown in Fig. 4D, the stronger green fluorescence of CRT can be seen in cells treated with FDR than in cells treated with FD and ART. Furthermore, the highest levels of ATP, HMGB1, and CRT in the FDRF group are found due to the FN-promoted cellular uptake (Fig. 4A–D), suggesting the tremendous ICD effect triggered by the FDRF NCs.

The DAMPs can trigger the maturation of DCs to activate T lymphocytes for immune-mediated tumor eradication [36]. For example, CRT transferring from rough endoplasmic reticulum to cytomembrane surface and HMGB1 spreading from the nucleus to the extracellular matrix can induce and speed up DCs maturation to express elevated levels of molecules involved in antigen presentation such as CD80 and CD86 [60,61].

As seen in Fig. 4E, to verify the DCs maturation *via* FDRF-induced ICD of 4T1 cells, the immature DCs (iDCs) were co-cultured with FDRF-treated 4T1 cells through a transwell system *in vitro*. Flow cytometry was used to analyze the biomarkers of DCs maturation, co-stimulatory molecules CD80 and CD86. Interestingly, the DCs in the FDR group show a maturity rate of 41.70%, about 2.6- and 8.0-fold higher than the ART and FD groups (Fig. 4F), respectively, owing to the improved ICD activation *via* the combined chemotherapy/enhanced CDT. Apparently, the highest maturity rate of 70.3% is observed in the FDRF group (Fig. 4F and Fig. S12), due to additional FN-mediated cancer cell targeting effect. Overall, the created FDRF NCs are able to successfully cause the ICD of 4T1 cells by the combination of chemotherapy and enhanced CDT, leading to the effective maturation of DCs *in vitro*.

3.9. T_1-weighted tumor MR imaging in vitro

Next, the developed FDRF NCs were used for T_1 MR imaging of a subcutaneous 4T1 tumor model *in vivo* after intravenous administration. The *in vivo* T_1-weighted MR images of tumors were captured at various time points post intravenous injection of FDRF or FDRB (Fig. 5A). The T_1 MR signal of tumors in the FDRF group is clearly stronger than that in the FDRB group (Fig. 5B) at 15, 30, and 45 min post-injection, proving that the FDRF NCs can enhance more positive MR contrast than the non-targeted control material of FDRB NCs. This could be ascribed to the FN-mediated active targeting. Moreover, the tumors treated with FDRF or FDRB show the peak T_1 MR signal intensity at 45 min post-injection (Fig. 5A–B and Fig. S13), owing to the most significant FDRF or FDRB ingestion at the tumor site. However, owing to the FN-mediated tumor targeting, the T_1 MR signal-to-noise ratio (SNR) of tumor site for the FDRF group is far higher than that for the FDRB group at 45 min post-injection ($p < 0.001$, Fig. S13). As time passes after injection, the FDRF and FDRB are gradually dissociated and metabolized, leading to an Fe-dependent decrease of T_1 MR signal at the tumor site. Apparently, the T_1 MR signals in the FDRB group can also be evidently found in other organs of mice due to the lack of targeting specificity (Fig. 5B). Collectively, the developed pH-responsive FDRF NCs can realize enhanced and targeted tumor T_1 MR imaging *in vivo*.

3.10. Cooperative chemo-chemodynamic-immune therapy

The ICB therapy targets regulatory pathways of T cells and breaks the immune escape of tumor cells with promoted antitumor immunity against the host immune system by employing the immune checkpoint inhibitor to interfere with the immunosuppressive signaling [62–64]. The A-PD-L1 has been selected as one most potent immune checkpoint inhibitor to be combined with a variety of therapeutic nanosystems for enhancing the immune response and efficient combination therapy of tumors [36,65,66]. Inspired by the excellent ICD efficacy *in vitro* derived from the FDRF-mediated combination anticancer treatment and the superiority of immunotherapy based on A-PD-L1, we constructed a

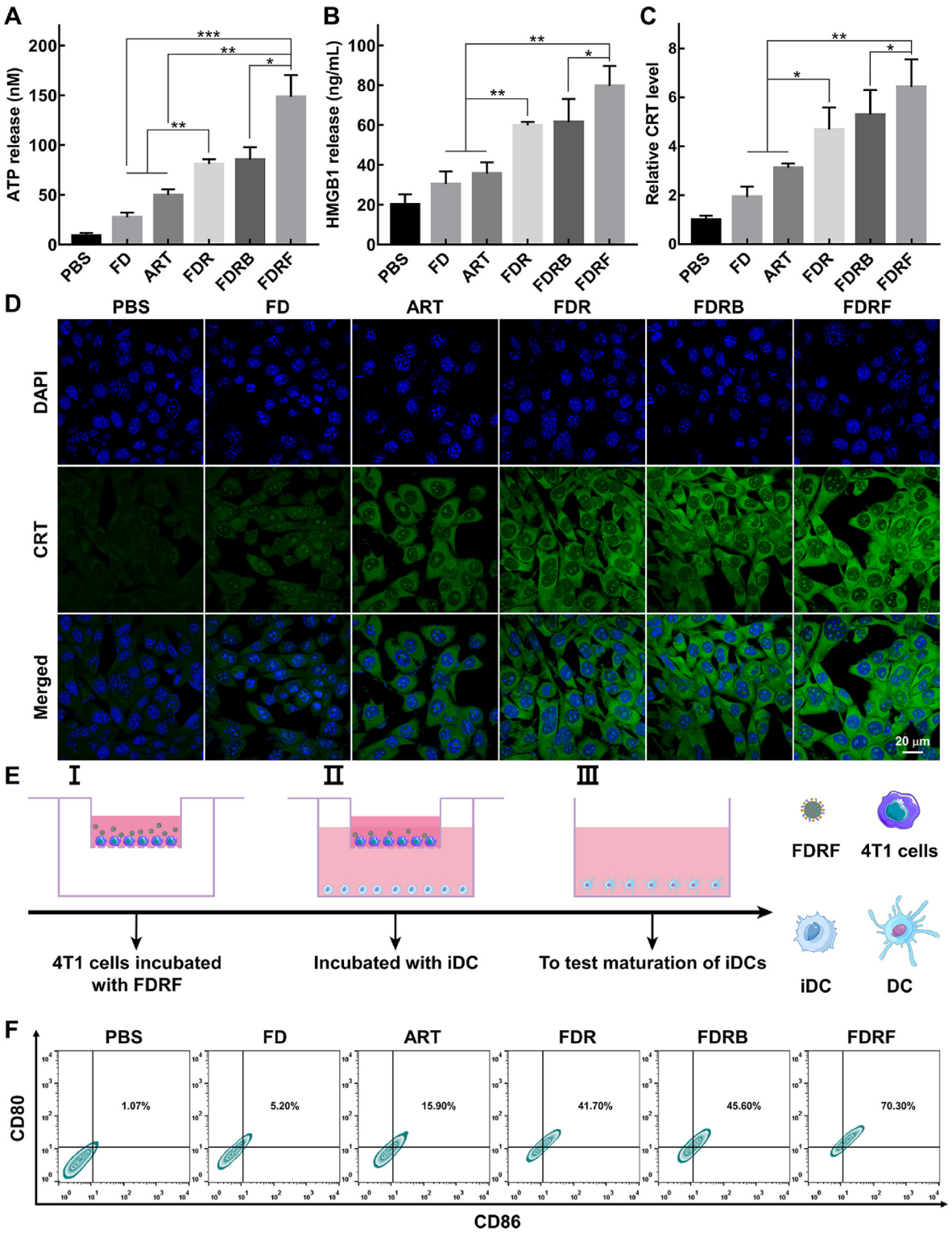

Fig. 4. ICD effect and DC maturation of FDRF NCs. (A) Extracellular ATP levels of 4T1 cells and (B) HMGB1 release from 4T1 cells after various treatments for 24 h (n = 3). (C) Quantitative analysis of CRT expression level from 4T1 cells after various treatments for 24 h. (D) Immunofluorescence imaging of CRT expression on the surface of 4T1 cells after different treatments as monitored *via* CLSM (scale bar = 20 μm). (E) The co-culture system of 4T1 cells and iDCs (I: 4T1 cells incubated with FDRF NCs, II: the treated 4T1 cells further incubated with iDC, III: assay of iDCs maturation). (F) Flow cytometry analysis of DC maturation after co-culture with the ICD 4T1 cells induced *via* various treatments. In parts A-C, * is for $p < 0.05$, ** is for $p < 0.01$, and *** is for $p < 0.001$, respectively.

subcutaneous xenografted 4T1 tumor model to evaluate the therapeutic efficacy of FDRF *in vivo via* the combination chemo-chemodynamic-immune therapy. According to the treatment timeline, the tumor-bearing mice were treated with PBS, FD, free ART, FDR, and FDRF, respectively. Furthermore, for the group of FDRF + A-PD-L1, the mice were intratumorally injected with A-PD-L1 (200 μg/mL, 100 μL for each mouse) every other day after treatment of FDRF (Fig. 5C). Compared to the FD and ART groups, the treatment of FDRF

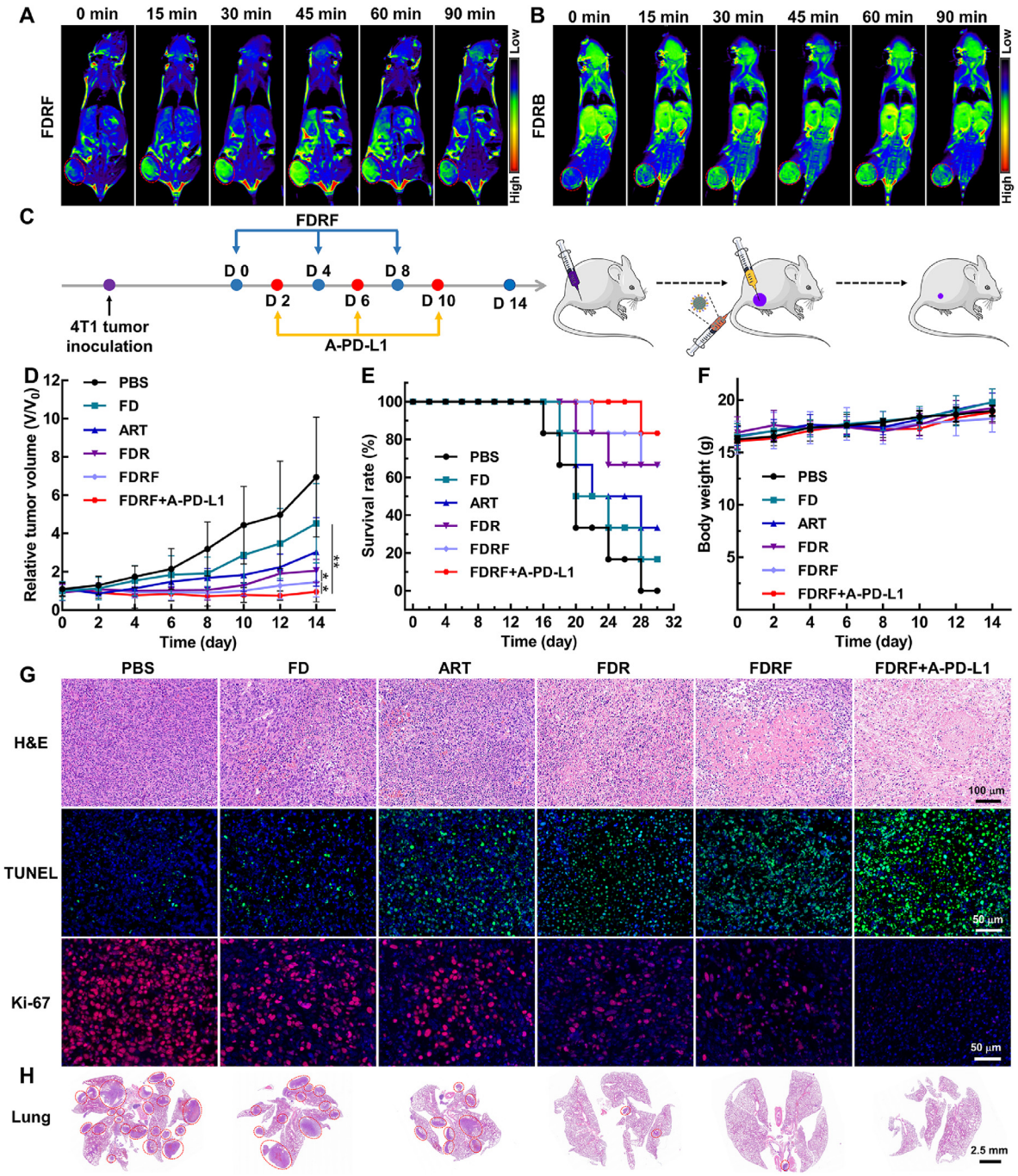

Fig. 5. MR imaging and therapy effect of FDRF NCs on 4T1 tumor. *In vivo* T_1-weighted MR images of tumors before and at different time points post intravenous injection of FDRF (A) or FDRB (B) ([Fe] = 400 μg·mL^{-1}, in 100 μL PBS for each mouse). (C) Timeline of the combined therapy using FDRF + A-PD-L1. (D) The relative tumor volumes, (E) the survival rates, and (F) the body weight changes of tumor-bearing mice after treatments by PBS, FD, free ART, FDR, FDRF, and FDRF + A-PD-L1 (n = 6) for different time periods. (G) Micrographs of tumor tissues stained by H&E, TUNEL and Ki-67 at 14 days post treatments in different groups (scale bar = 100 μm or 50 μm). (H) H&E staining of the lung from tumor-bearing mice after various treatments for 14 days (scale bar = 2.5 mm). In part D, * is for $p < 0.05$, and ** is for $p < 0.01$, respectively.

results in the significant suppression of tumors, owing to both FN-mediated targeting and the combination of chemotherapy and enhanced CDT (Fig. 5D and Fig. S14). Obviously, the tri-mode combination therapy uniting the ICB (FDRF + A-PD-L1) leads to the maximal tumor inhibitory effect, which can be further proved by the highest survival rate (83.3%) until 30 days. To be contrasted, the survival rates of PBS, FD, and free ART groups are less than or equal to 33.3% at the same time period (Fig. 5E). In addition, the good biosafety profiles of NCs and ART are proved by steady body weight changes of mice after different treatments throughout the experimental period (Fig. 5F).

Moreover, to evaluate the efficacy of FDRF + A-PD-L1 for combined chemo-chemodynamic-immune therapy, the tumor slices in different groups were H&E, TUNEL and Ki-67 stained (Fig. 5G). The FDRF + A-PD-L1 group shows the most effective tumor necrosis, apoptosis, and proliferation inhibition effects among all groups, proving the great advantages of the FDRF + A-PD-L1-mediated tri-mode combination therapy.

Additional H&E staining and photograph of lung of tumor-bearing mice (Fig. 5H and Fig. S15) show that the lung metastases are mainly observed in the groups of PBS, FD, and free ART. Much more lung metastasis nodules can be seen in the PBS, FD, and free ART groups than in the other groups ($p < 0.05$), whereas the lung metastasis nodules are hardly detected in the FDRF + A-PD-L1 group (Fig. S15). Overall, the combination therapy is most effective in treatment of both primary tumor and tumor metastasis among all treatment groups.

To validate the improved TME remodeling *in vivo* by the combination therapy, the tumor slices were stained by DCFH-DA to explore the ROS level, and immunofluorescencely stained to examine the expression of CRT for confirmation of the ICD effect *in vivo*, respectively. As seen in Fig. S16A, the treatment of FDR results in a remarkable increase of red fluorescence, suggesting the increased expression of ROS in tumor cells after the combined chemotherapy and enhanced CDT. The red fluorescence intensity of the FDRF group further increases due to the FN-mediated tumor targeting. The highest ROS level can be observed in the FDRF + A-PD-L1 group, demonstrating that the FDRF + A-PD-L1-mediated tri-mode combination therapy can promote ROS generation in tumor cells *in vivo*. Likewise, the FDR NCs can enhance CRT level of tumor cells to a certain degree, while the FDRF and FDRF + A-PD-L1 can evoke a more pronounced CRT expression than other materials (Fig. S16B), proving the enhanced tumor cell ICD effect *via* the targeted combination therapy.

We next explored the DCs maturation and T cells intratumoral infiltration to confirm the immune activation of FDRF + A-PD-L1 in tumor immune microenvironment through immunofluorescence staining. Clearly, the FDRF + A-PD-L1-mediated tri-mode combo therapy induces evident maturation of DCs with high expression of $CD80^+$ and $CD86^+$ (Fig. S17). Since the mature DCs can present tumor antigen to further activate tumor-specific T cell immunity [59], we then checked the T cells infiltrated in tumors. As shown in Fig. 6A, the $CD4^+$ helper T cells and $CD8^+$ cytotoxic T cells infiltrating and accumulating in the tumors are more significantly upregulated in the FDRF+A-PD-L1 group than the other groups. Similarly, as can be seen in Fig. S18, the $CD4^+$ helper T cells and $CD8^+$ cytotoxic T cells in spleen are also more profoundly

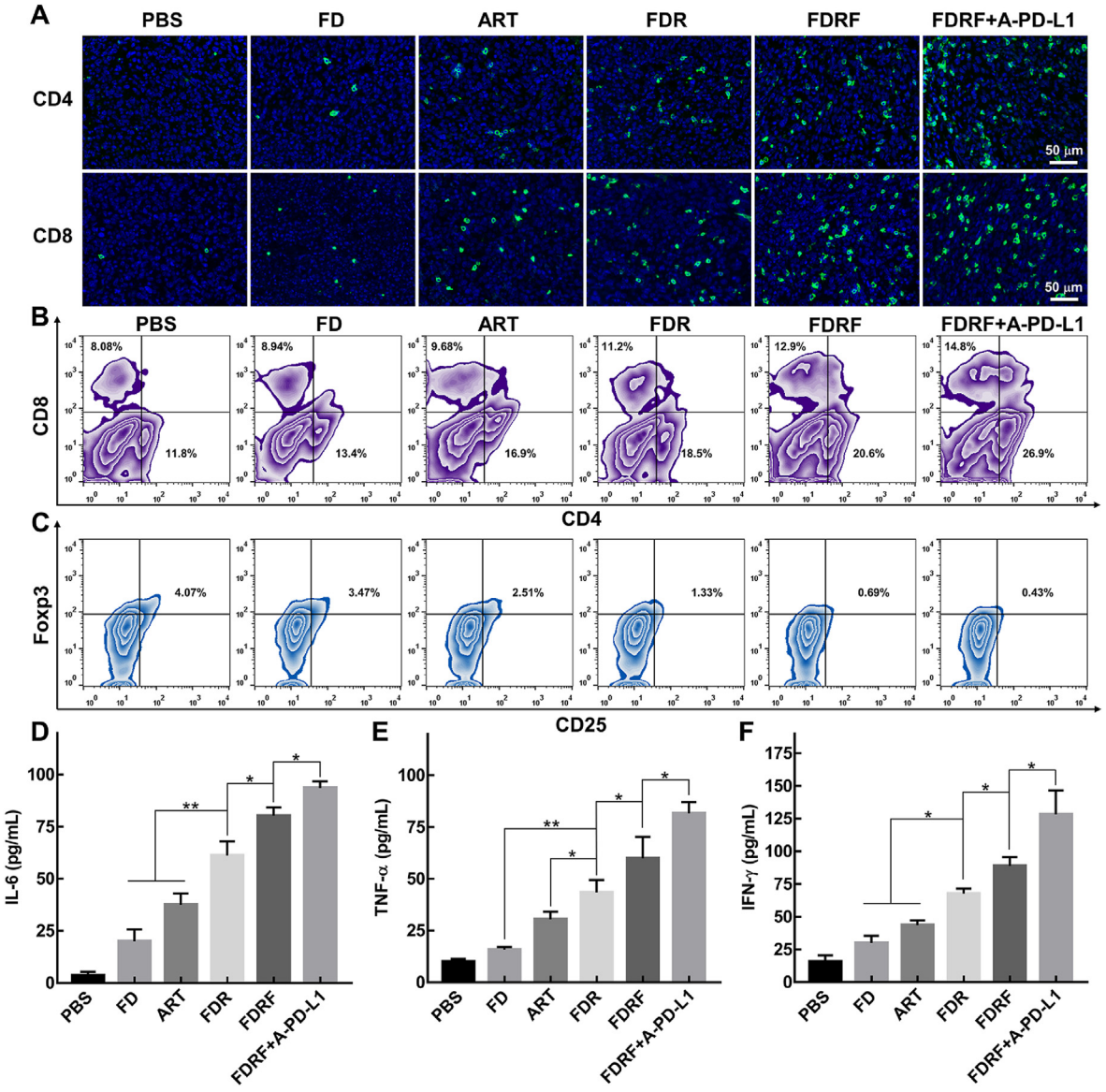

Fig. 6. Antitumor immune response of the FDRF NCs combined with A-PD-L1. (A) Immunofluorescence staining of $CD4^+$ T cells and $CD8^+$ T cells in tumor slices after different treatments for 14 days (scale bar = 50 μm). Flow cytometry plots indicating the proportions of (B) $CD4^+$ and $CD8^+$ T cells, and (C) Tregs ($CD4^+CD25^+Foxp3^+$ T cells) in tumors after various treatments for 14 days (n = 3). Cytokine levels of IL-6 (D), TNF-α (E), and IFN-γ (F) in the serum of tumor-bearing mice after various treatments for 14 days. In parts D-F, * is for $p < 0.05$, and ** is for $p < 0.01$, respectively (n = 3).

upregulated in the FDRF+A-PD-L1 group than the other groups ($p < 0.05$). Quantitatively, the infiltration rates of $CD4^+$ and $CD8^+$ T cells in the FDRF+A-PD-L1 group are 26.9% and 14.8%, respectively, which are higher than those in the other groups (Fig. 6B), likely attributed to the FDRF-induced maturation of DCs and A-PD-L1-mediated ICB. Meanwhile, the most remarkable downregulation of intratumoral immunosuppressive regulatory T cells (Tregs) expressing $CD4^+CD25^+Foxp3^+$ can be observed (0.43%) in the group of FDRF + A-PD-L1 among all groups (Fig. 6C). The above results imply that the treatment of FDRF NCs significantly induces the antitumor immune response after combination with the A-PD-L1-mediated ICB in terms of DCs maturation and T cells infiltration in tumors.

In addition, the enzyme-linked immunosorbent assays were employed to analyze the T cell-derived cytokines including interleukin-6 (IL-6) and interferon-γ (IFN-γ), and the monocytes- and macrophages-derived cytokine of tumor necrosis factor-α (TNF-α). As shown in Fig. 6D–F, the treatment of FDRF can more significantly upregulate the levels of IL-6, TNF-α, and IFN-γ than those of FD ($p < 0.01$), ART ($p < 0.01$), and FDR ($p < 0.05$). Compared to the FDRF groups ($p < 0.05$), the FDRF + A-PD-L1 group displays a higher secretion of IFN-γ, TNF-α, and IL-6, indicating a robust immune response through the combination of FDRF-triggered ICD and adjunctive A-PD-L1-mediated ICB. Overall, our results suggest that the FDRF combined with A-PD-L1 can successfully induce both DCs maturation, T cells activation, and Tregs downregulation to reverse the TME for enhanced antitumor immunotherapy.

3.11. Biosafety evaluation in vivo

To validate the biosafety of FDRF NCs, the percentage of Fe per gram of tissue was measured to investigate the time-dependent Fe distribution in tumor-bearing mice. As shown in Fig. S19A, the FDRF group shows a large amount of Fe taken up by the heart, liver, spleen, lung, and kidney at 90 min post-injection, and the highest amount of Fe in the lung at 60 min post-injection among the investigated time points. The Fe contents in the corresponding organs in the FDRF group are much lower than those in the FDRB group (Fig. S19B). The peak tumor Fe content in the FDRF group can be seen at 45 min post-injection (Fig. S19A), which is much higher than that in the FDRB group (Fig. S19B), likely attributed to the FN-mediated active tumor targeting. Subsequently, in all organs and tumors, the uptake of Fe gradually decreases to be more or less similar to the control with the time post injection for both FDRF and FDRB groups. These results indicate that the accumulation of FDRF in tumors can be largely improved by FN-mediated targeting, and the FDRF NCs can be progressively eliminated *via* a normal metabolization process. Moreover, after different treatments, there are no significant pathological damage and inflammation infiltration in the H&E stained major organs (heart, liver, spleen, and kidney) of tumor-bearing mice (Fig. S20), implying the desired biosafety of FDRF NCs and all other materials. Lastly, we performed the blood routines and serum biochemistry assays to further comprehensively evaluate the biosafety of FDRF NCs after the tumor treatments. As shown in Fig. S21, all measured parameters are within the normal ranges in all groups with no significant differences observed between the FDRF + A-PD-L1 group and other groups, proving the excellent biosafety of FDRF NCs.

4. Conclusions

We developed a versatile nanoplatform based on ART/FN-loaded FD NCs by a microfluidic synthesis method for T_1 MR imaging-guided tumor chemotherapy/CDT/immune therapy. The FD NCs formed by assembly of DA and Fe^{2+} can be further physically loaded with ART and chemically coated with FN through controlling reaction conditions based on tunable microfluidics. The developed FDRF NCs with a size of 161.0 nm show good colloidal stability, homogeneity, r_1 relaxivity (4.96 $mM^{-1}s^{-1}$), pH-dependent Fe and ART release profiles, and self-supplementing TME regulation through ROS production and GSH depletion. In particular, through the Fe^{2+}-mediated ART reduction/Fenton reaction and Fe^{3+}-mediated GSH oxidation in TME, self-supplementing and sustained TME regulation can be realized by a classic cycling reaction between Fe^{2+} and Fe^{3+}. Meanwhile, the FDRF NCs can induce the ICD effect of cancer cells by Fe^{2+}/ART-induced enhanced CDT and ART-mediated chemotherapy, triggering the maturation of DCs to activate T lymphocytes for immune therapy. The combined A-PD-L1-mediated ICB enables further enhanced T cell-based antitumor immune response, improving the efficacy of tumor therapy *in vivo*. Owing to the FN-mediated tumor targeting and pH-responsive enhancement of r_1 relaxivity (5.93 $mM^{-1}s^{-1}$) in TME, the created FDRF NCs could be developed as a promising theranostic nanoplatform for precision T_1 MR imaging-guided tumor combination therapy, potentially translating for clinical applications.

Credit author statement

Rui Yang: Methodology, Investigation, Data curation, Validation, Formal analysis, Writing - original draft. **Mengsi Zhan:** Methodology, Investigation, Data curation, Formal analysis. **Zhijun Ouyang:** Methodology, Investigation, Data curation. **Honghua Guo:** Methodology, Investigation, Data curation. **Jiao Qu:** Methodology, Investigation, Data curation. **Jindong Xia:** Supervision, Resources. **Mingwu Shen:** Supervision, Resources, Funding acquisition, Project administration. **Xiangyang Shi:** Conceptualization, Supervision, Resources, Funding acquisition, Project administration, Writing-review & editing.

Declaration of competing interest

The authors declare that they have no known competing financial interests or personal relationships that could have appeared to influence the work reported in this paper.

Data availability

Data will be made available on request.

Acknowledgements

This study was financially supported by the National Key R&D Program (2022YFE0196900), the Science and Technology Commission of Shanghai Municipality (20520710300, 21490711500 and 20DZ2254900), the Shanghai Education Commission through the Shanghai Leading Talents Program, and the 111 Project (BP0719035).

Appendix A. Supplementary data

Supplementary data to this article can be found online at https://doi.org/10.1016/j.mtbio.2023.100670.

References

[1] B. Hassannia, P. Vandenabeele, T. Vanden Berghe, Targeting ferroptosis to iron out cancer, Cancer Cell 35 (2019) 830–849.
[2] J. Bariwal, H. Ma, G.A. Altenberg, H. Liang, Nanodiscs: a versatile nanocarrier platform for cancer diagnosis and treatment, Chem. Soc. Rev. 51 (2022) 1702–1728.
[3] J. Peng, Q. Yang, K. Shi, Y. Xiao, X. Wei, Z. Qian, Intratumoral fate of functional nanoparticles in response to microenvironment factor: implications on cancer diagnosis and therapy, Adv. Drug Deliv. Rev. 143 (2019) 37–67.
[4] S. Yan, P. Sun, N. Niu, Z. Zhang, W. Xu, S. Zhao, L. Wang, D. Wang, B.Z. Tang, "One stone, four birds" ion engineering to fabricate versatile core-shell organosilica nanoparticles for intelligent nanotheranostics, ACS Nano 16 (2022) 9785–9798.
[5] A. Zhang, Q. Zhang, G. Alfranca, S. Pan, Z. Huang, J. Cheng, Q. Ma, J. Song, Y. Pan, J. Ni, L. Ma, D. Cui, GSH-triggered sequential catalysis for tumor imaging and eradication based on star-like Au/Pt enzyme carrier system, Nano Res. 13 (2020) 160–172.
[6] H.-R. Jia, Y.-X. Zhu, X. Liu, G.-Y. Pan, G. Gao, W. Sun, X. Zhang, Y.-W. Jiang, F.-G. Wu, Construction of dually responsive nanotransformers with nanosphere-nanofiber-nanosphere transition for overcoming the size paradox of anticancer nanodrugs, ACS Nano 13 (2019) 11781–11792.

[7] Y. Zhou, S. Fan, L. Feng, X. Huang, X. Chen, Manipulating intratumoral fenton chemistry for enhanced chemodynamic and chemodynamic-synergized multimodal therapy, Adv. Mater. 33 (2021), 2104223.

[8] D. Li, R. Zhang, G. Liu, Y. Kang, J. Wu, Redox-responsive self-assembled nanoparticles for cancer therapy, Adv. Healthcare Mater. 9 (2020), 2000605.

[9] Z. Tang, Y. Liu, M. He, W. Bu, Chemodynamic therapy: tumour microenvironment-mediated fenton and fenton-like reactions, Angew. Chem., Int. Ed. 58 (2019) 946–956.

[10] C. Zhang, W. Bu, D. Ni, S. Zhang, Q. Li, Z. Yao, J. Zhang, H. Yao, Z. Wang, J. Shi, Synthesis of iron nanometallic glasses and their application in cancer therapy by a localized fenton reaction, Angew. Chem., Int. Ed. 55 (2016) 2101–2106.

[11] L. Lin, S. Wang, H. Deng, W. Yang, L. Rao, R. Tian, Y. Liu, G. Yu, Z. Zhou, J. Song, H.-H. Yang, Z.-Y. Chen, X. Chen, Endogenous labile iron pool-mediated free radical generation for cancer chemodynamic therapy, J. Am. Chem. Soc. 142 (2020) 15320–15330.

[12] Y. Zhuang, S. Han, Y. Fang, H. Huang, J. Wu, Multidimensional transitional metal-actuated nanoplatforms for cancer chemodynamic modulation, Coord. Chem. Rev. 455 (2022), 214360.

[13] P. Mi, Stimuli-responsive nanocarriers for drug delivery, tumor imaging, therapy and theranostics, Theranostics 10 (2020) 4557–4588.

[14] C. Li, J. Xia, X. Wei, H. Yan, Z. Si, S. Ju, pH-activated near-infrared fluorescence nanoprobe imaging tumors by sensing the acidic microenvironment, Adv. Funct. Mater. 20 (2010) 2222–2230.

[15] M. Giorgio, M. Trinei, E. Migliaccio, P.G. Pelicci, Hydrogen peroxide: a metabolic by-product or a common mediator of ageing signals? Nat. Rev. Mol. Cell Biol. 8 (2007) 722–728.

[16] J. Zhang, C. Liang, Z. Wei, W. Yang, W. Ge, X. Qu, W. Si, W. Wang, X. Mou, X. Dong, TME-triggered $MnSiO_3$@Met@GOx nanosystem for ATP dual-inhibited starvation/chemodynamic synergistic therapy, Biomaterials 287 (2022), 121682.

[17] N. Zhang, G. Shu, L. Shen, J. Ding, E. Qiao, S. Fang, J. Song, Y. Yang, Z. Zhao, C. Lu, J. Tu, M. Xu, Y. Du, M. Chen, J. Ji, Biomimetic mesoporous polydopamine nanoparticles for MRI-guided photothermal-enhanced synergistic cascade chemodynamic cancer therapy, Nano Res. 15 (2022) 5262–5272.

[18] Y. Xu, Y. Guo, C. Zhang, M. Zhan, L. Jia, S. Song, C. Jiang, M. Shen, X. Shi, Fibronectin-coated metal-phenolic networks for cooperative tumor chemo/chemodynamic/immune therapy *via* enhanced ferroptosis-mediated immunogenic cell death, ACS Nano 16 (2022) 984–996.

[19] T. Xiao, M. He, F. Xu, Y. Fan, B. Jia, M. Shen, H. Wang, X. Shi, Macrophage membrane-camouflaged responsive polymer nanogels enable magnetic resonance imaging-guided chemotherapy/chemodynamic therapy of orthotopic glioma, ACS Nano 15 (2021) 20377–20390.

[20] H. Zhang, L. Hou, X. Jiao, Y. Ji, X. Zhu, Z. Zhang, Transferrin-mediated fullerenes nanoparticles as Fe^{2+}-dependent drug vehicles for synergistic anti-tumor efficacy, Biomaterials 37 (2015) 353–366.

[21] S. Xiang, Z. Fan, Z. Ye, T. Zhu, D. Shi, S. Ye, Z. Hou, X. Chen, Endogenous Fe^{2+}-activated ROS nanoamplifier for esterase-responsive and photoacoustic imaging-monitored therapeutic improvement, Nano Res. 15 (2022) 907–918.

[22] Z. Fan, B. Jiang, Q. Zhu, S. Xiang, L. Tu, Y. Yang, Q. Zhao, D. Huang, J. Han, G. Su, D. Ge, Z. Hou, Tumor-specific endogenous Fe-II-activated, MRI-guided self-targeting gadolinium-coordinated theranostic nanoplatforms for amplification of ROS and enhanced chemodynamic chemotherapy, ACS Appl. Mater. Inter. 12 (2020) 14884–14904.

[23] D. Wang, I.W. He, J. Liu, D. Jana, Y. Wu, X. Zhang, C. Qian, Y. Guo, X. Chen, A.K. Bindra, Y. Zhao, Missing-linker-assisted artesunate delivery by metal-organic frameworks for synergistic cancer treatment, Angew. Chem., Int. Ed. 60 (2021) 26254–26259.

[24] S.A. Amolegbe, H. Ohmagari, K. Wakata, H. Takehira, R. Ohtani, M. Nakamura, C. Yu, S. Hayami, Synthesis of mesoporous materials as nano-carriers for an antimalarial drug, J. Mater. Chem. B 4 (2016) 1040–1043.

[25] J. Chen, X. Wang, Y. Zhang, S. Zhang, H. Liu, J. Zhang, H. Feng, B. Li, X. Wu, Y. Gao, B. Yang, A redox-triggered C-centered free radicals nanogenerator for self-enhanced magnetic resonance imaging and chemodynamic therapy, Biomaterials 266 (2021), 120457.

[26] P. Xie, Q. Jin, Y. Li, J. Zhang, X. Kang, J. Zhu, X. Mao, P. Cao, C. Liu, Nanoparticle delivery of a triple-action Pt(iv) prodrug to overcome cisplatin resistance via synergistic effect, Biomater. Sci. 10 (2021) 153–157.

[27] S. Zhang, H. Yuan, Y. Guo, K. Wang, X. Wang, Z. Guo, Towards rational design of RAD51-targeting prodrugs: platinum(IV)-artesunate conjugates with enhanced cytotoxicity against BRCA-proficient ovarian and breast cancer cells, Chem. Commun. 54 (2018) 11717–11720.

[28] L. Liu, Y. Wei, S. Zhai, Q. Chen, D. Xing, Dihydroartemisinin and transferrin dual-dressed nano-graphene oxide for a pH-triggered chemotherapy, Biomaterials 62 (2015) 35–46.

[29] J. Bai, X. Jia, W. Zhen, W. Cheng, X. Jiang, A facile ion-doping strategy to regulate tumor microenvironments for enhanced multimodal tumor theranostics, J. Am. Chem. Soc. 140 (2018) 106–109.

[30] S.J. Dixon, K.M. Lemberg, M.R. Lamprecht, R. Skouta, E.M. Zaitsev, C.E. Gleason, D.N. Patel, A.J. Bauer, A.M. Cantley, W.S. Yang, B. Morrison III, B.R. Stockwell, Ferroptosis: an iron-dependent form of nonapoptotic cell death, Cell 149 (2012) 1060–1072.

[31] C. Xu, Y. Yu, Y. Sun, L. Kong, C. Yang, M. Hu, T. Yang, J. Zhang, Q. Hu, Z. Zhang, Transformable nanoparticle-enabled synergistic elicitation and promotion of immunogenic cell death for triple-negative breast cancer immunotherapy, Adv. Funct. Mater. 29 (2019), 1905213.

[32] X. Zhao, K. Guo, K. Zhang, S. Duan, M. Chen, N. Zhao, F.-J. Xu, Orchestrated yolk-shell nanohybrids regulate macrophage polarization and dendritic cell maturation for oncotherapy with augmented antitumor immunity, Adv. Mater. 34 (2022), 2108263.

[33] H. Yu, Y. Li, Z. Zhang, J. Ren, L. Zhang, Z. Xu, Y. Kang, P. Xue, Silk fibroin-capped metal-organic framework for tumor-specific redox dyshomeostasis treatment synergized by deoxygenation-driven chemotherapy, Acta Biomater. 138 (2022) 545–560.

[34] K. Yang, S. Qi, X. Yu, B. Bai, X. Zhang, Z. Mao, F. Huang, G. Yu, A hybrid supramolecular polymeric nanomedicine for cascade-amplified synergetic cancer therapy, Angew. Chem., Int. Ed. 61 (2022), e202203786.

[35] L. Xie, G. Wang, W. Sang, J. Li, Z. Zhang, W. Li, J. Yan, Q. Zhao, Y. Dai, Phenolic immunogenic cell death nanoinducer for sensitizing tumor to PD-1 checkpoint blockade immunotherapy, Biomaterials 269 (2021), 120638.

[36] Z. Zhang, W. Sang, L. Xie, W. Li, B. Li, J. Li, H. Tian, Z. Yuan, Q. Zhao, Y. Dai, Polyphenol-based nanomedicine evokes immune activation for combination cancer treatment, Angew. Chem., Int. Ed. 60 (2021) 1967–1975.

[37] N. Wang, C. Liu, Z. Lu, W. Yang, L. Li, S. Gong, T. He, C. Ou, L. Song, M. Shen, Q. Wu, C. Gong, Multistage sensitive nanoCRISPR enable efficient intracellular disruption of immune checkpoints for robust innate and adaptive immune coactivation, Adv. Funct. Mater. 30 (2020), 2004940.

[38] K. Ni, T. Aung, S. Li, N. Fatuzzo, X. Liang, W. Lin, Nanoscale metal-organic framework mediates radical therapy to enhance cancer immunotherapy, Chem 5 (2019) 1892–1913.

[39] J. Xing, T. Mei, K. Luo, Z. Li, A. Yang, Z. Li, Z. Xie, Z. Zhang, S. Dong, T. Hou, J. Xu, F. Luo, A nano-scaled and multi-layered recombinant fibronectin/cadherin chimera composite selectively concentrates osteogenesis-related cells and factors to aid bone repair, Acta Biomater. 53 (2017) 470–482.

[40] L. Hao, T. Li, L. Wang, X. Shi, Y. Fan, C. Du, Y. Wang, Mechanistic insights into the adsorption and bioactivity of fibronectin on surfaces with varying chemistries by a combination of experimental strategies and molecular simulations, Bioact. Mater. 6 (2021) 3125–3135.

[41] A. Oyane, M. Murayama, A. Yamazaki, Y. Sogo, A. Ito, H. Tsurushima, Fibronectin-DNA-apatite composite layer for highly efficient and area-specific gene transfer, J. Biomed. Mater. Res., Part A 92A (2010) 1038–1047.

[42] M. Izci, C. Maksoudian, B.B. Manshian, S.J. Soenen, The use of alternative strategies for enhanced nanoparticle delivery to solid tumors, Chem. Rev. 121 (2021) 1746–1803.

[43] X. Zhao, F. Bian, L. Sun, L. Cai, L. Li, Y. Zhao, Microfluidic generation of nanomaterials for biomedical applications, Small 16 (2020), 1901943.

[44] L.-L. Li, X. Li, H. Wang, Microfluidic synthesis of nanomaterials for biomedical applications, Small Methods 1 (2017), 1700140.

[45] D. Liu, H. Zhang, E. Makila, J. Fan, B. Herranz-Blanco, C.-F. Wang, R. Rosa, A.J. Ribeiro, J. Salonen, J. Hirvonen, H.A. Santos, Microfluidic assisted one-step fabrication of porous silicon@acetalated dextran nanocomposites for precisely controlled combination chemotherapy, Biomaterials 39 (2015) 249–259.

[46] L. Uson, M. Arruebo, V. Sebastian, J. Santamaria, Single phase microreactor for the continuous, high-temperature synthesis of $<$ 4 nm superparamagnetic iron oxide nanoparticles, Chem. Eng. J. 340 (2018) 66–72.

[47] S.J. Shepherd, D. Issadore, M.J. Mitchell, Microfluidic formulation of nanoparticles for biomedical applications, Biomaterials 274 (2021), 120826.

[48] C. Liu, Q. Feng, J. Sun, Lipid nanovesicles by microfluidics: manipulation, synthesis, and drug delivery, Adv. Mater. 31 (2019), 1804788.

[49] H. Zhang, Y. Zhu, Y. Shen, Microfluidics for cancer nanomedicine: from fabrication to evaluation, Small 14 (2018), 1800360.

[50] C. Liu, W. Zhang, Y. Li, J. Chang, F. Tian, F. Zhao, Y. Ma, J. Sun, Microfluidic sonication to assemble exosome membrane-coated nanoparticles for immune evasion-mediated targeting, Nano Lett. 19 (2019) 7836–7844.

[51] R. Karnik, F. Gu, P. Basto, C. Cannizzaro, L. Dean, W. Kyei-Manu, R. Langer, O.C. Farokhzad, Microfluidic platform for controlled synthesis of polymeric nanoparticles, Nano Lett. 8 (2008) 2906–2912.

[52] L. Zhang, J.S. Sun, Y.L. Wang, J.C. Wang, X.H. Shi, G.Q. Hu, Nonspecific organelle-targeting strategy with core-shell nanoparticles of varied lipid components/ratios, Anal. Chem. 88 (2016) 7344–7351.

[53] L. Zhang, Q. Feng, J.L. Wang, J.S. Sun, X.H. Shi, X.Y. Jiang, Microfluidic synthesis of rigid nanovesicles for hydrophilic reagents delivery, Angew. Chem., Int. Ed. 54 (2015) 3952–3956.

[54] Q. Feng, J. Liu, X. Li, Q. Chen, J. Sun, X. Shi, B. Ding, H. Yu, Y. Li, X. Jiang, One-step microfluidic synthesis of nanocomplex with tunable rigidity and acid-switchable surface charge for overcoming drug resistance, Small 13 (2017), 1603109.

[55] Z. Wang, Y. Zou, Y. Li, Y. Cheng, Metal-containing polydopamine nanomaterials: catalysis, energy, and theranostics, Small 16 (2020), 1907042.

[56] Y. Zhu, N. Xin, Z. Qiao, S. Chen, L. Zeng, Y. Zhang, D. Wei, J. Sun, H. Fan, Novel tumor-microenvironment-based sequential catalytic therapy by Fe(II)-engineered polydopamine nanoparticles, ACS Appl. Mater. Inter. 11 (2019) 43018–43030.

[57] B. Niu, K. Liao, Y. Zhou, T. Wen, G. Quan, X. Pan, C. Wu, Application of glutathione depletion in cancer therapy: enhanced ROS-based therapy, ferroptosis, and chemotherapy, Biomaterials 277 (2021), 121110.

[58] Y. Xiong, C. Xiao, Z. Li, X. Yang, Engineering nanomedicine for glutathione depletion-augmented cancer therapy, Chem. Soc. Rev. 50 (2021) 6013–6041.

[59] G. Hou, W. Xu, M. Guo, J. Wang, Y. Wang, A. Suo, J. Qian, Full-active Cu_2O/drug core/shell nanoparticles based on "grafting from" drug coordination polymerization combined with PD-1 blockade for efficient cancer therapy, Chem. Eng. J. 441 (2022), 135993.

[60] W. Qiu, M. Liang, Y. Gao, X. Yang, X. Zhang, X. Zhang, P. Xue, Y. Kang, Z. Xu, Polyamino acid calcified nanohybrids induce immunogenic cell death for augmented chemotherapy and chemo-photodynamic synergistic therapy, Theranostics 11 (2021) 9652–9666.

[61] J. Wei, D. Wu, S. Zhao, Y. Shao, Y. Xia, D. Ni, X. Qiu, J. Zhang, J. Chen, F. Meng, Z. Zhong, Immunotherapy of malignant glioma by noninvasive administration of TLR9 agonist CpG nano-immunoadjuvant, Adv. Sci. 9 (2022), 2103689.
[62] J. Choi, M.K. Shim, S. Yang, H.S. Hwang, H. Cho, J. Kim, W.S. Yun, Y. Moon, J. Kim, H.Y. Yoon, K. Kim, Visible-light-triggered prodrug nanoparticles combine chemotherapy and photodynamic therapy to potentiate checkpoint blockade cancer immunotherapy, ACS Nano 15 (2021) 12086–12098.
[63] M. Nishino, N.H. Ramaiya, H. Hatabu, F.S. Hodi, Monitoring immune-checkpoint blockade: response evaluation and biomarker development, Nat. Rev. Clin. Oncol. 14 (2017) 655–668.
[64] A.F. Haddad, J.S. Young, S. Gill, M.K. Aghi, Resistance to immune checkpoint blockade: mechanisms, counter-acting approaches, and future directions, Semin. Cancer Biol. 86 (2022) 532–541.
[65] R. Guo, S. Wang, L. Zhao, Q. Zong, T. Li, G. Ling, P. Zhang, Engineered nanomaterials for synergistic photo-immunotherapy, Biomaterials 282 (2022), 121425.
[66] X. Xiao, S. Liang, Y. Zhao, M. Pang, P.a. Ma, Z. Cheng, J. Lin, Multifunctional carbon monoxide nanogenerator as immunogenic cell death drugs with enhanced antitumor immunity and antimetastatic effect, Biomaterials 277 (2021), 121120.